

# Achieving High Energy Storage Density at Low Operating Fields in Lead Hafnate-Based Novel Perovskite Solid Solutions

Journal:	Journal of Materials Chemistry A
Manuscript ID	TA-ART-04-2024-002493.R3
Article Type:	Paper
Date Submitted by the Author:	09-Sep-2024
Complete List of Authors:	Chauhan, Vidhi; Simon Fraser University Wang, Bi-Xia; Simon Fraser University Bokov, Alexei; Simon Fraser University, Chemistry Ye, Zuo-Guang; Simon Fraser University, Chemistry

SCHOLARONE™ Manuscripts

# **ARTICLE**

# Achieving High Energy Storage Density at Low Operating Fields in Lead Hafnate-Based Novel Perovskite Solid Solutions

Received 00th January 20xx, Accepted 00th January 20xx

DOI: 10.1039/x0xx00000x

Vidhi Chauhan, Bi-Xia Wang, Alexei A. Bokov and Zuo-Guang Ye\*

Miniaturization and integration of pulse power capacitors has become a backbone of modern technology. Antiferroelectric (AFE) perovskite materials with high recoverable energy-storage density ( $W_{rec}$ ) at a low operating electric field can meet such a demand. To increase  $W_{rec}$  at low operating voltages a novel solid solution of (1-x)PbHfO<sub>3</sub>-xAgNbO<sub>3</sub> ( $0 \le x \le 0.03$ ) between AFE and a ferrielectric perovskites is synthesized via a cost-effective solid-state synthesis route. A temperature-composition phase diagram is constructed based on x-ray diffraction, dielectric and ferroelectric measurements. At room temperature, all the compositions are found to crystallize in an orthorhombic symmetry with the Pbam space group and demonstrate AFE properties. Upon heating the phase transition to another orthorhombic AFE phase with the Imma space group is observed. For the compositions of  $x \ge 0.03$ , a third AFE phase with Imma space group is found. At room temperature an optimal energy-storage performance is obtained at x = 0.027 with  $W_{rec} = 4.8$  J/cm³ and an efficiency of 58% at an electric field of 172 kV/cm. Such a performance is superior to all the perovskite ceramics so far reported under a similar or lower electric field. Furthermore, all the compositions exhibit good energy storage performance up to temperatures as high as 175 °C, which makes them viable materials for high temperature applications at low operating fields.

# 1. Introduction

Due to the extensive use of fossil fuel causing global warming, climate changes and environmental pollution, a sustainable development of human society is in a precarious position. 1-5 Therefore, development of green energy has been a global challenge. Along with the green energy production the issue of energy storage becomes increasingly important. According to the document "Energy Storage Grand Challenge: Energy Storage Market Report" by the U.S. Department of Energy, the demand for energy storage will increase to be more than 2500 GWh by the end of year 2030. <sup>6</sup> To meet such a requirement, it is necessary to develop new and more advanced technologies for energy storage. For decades, dielectrics have been playing a vital role in the fields of pulse power generation, electrocaloric cooling and solar cells. <sup>7-9</sup> In recent years, needs for devices with better stability and safety, and possibility of miniaturization have been driving the investigations of dielectrics with high energy density. According to the Ragone plot of typical energy storage devices, presently available energy storage devices like flywheels, electrochemical capacitors, superconducting magnets possess a high enough energy density, but unfortunately, very low power density. 9-10 On the other hand, dielectric capacitors which store energy electrostatically, have high-power density, rapid chargedischarge capability and good thermal stability, but inferior energy storage density. 11-13 To meet the demand of compactness and integration, it is important to increase the energy storage capabilities, especially the energy density of dielectric capacitors at low operating voltages. Among the four

main types of dielectric capacitor materials, namely, linear dielectrics, ferroelectrics (FE), relaxors and antiferroelectrics (AFE), AFE materials are the most promising class of materials for the purpose due to the double polarization-electric field (P-E) hysteresis loop arising from the electric field-induced AFE to FE phase transition. 14 To design and engineer a good AFE material, it is important to understand its energy storage mechanism. Figure 1 demonstrates the energy storage mechanism of AFEs. A dielectric capacitor is composed of two conductive plates with an AFE dielectric in between. In AFE dielectrics, the neighbouring local dipoles are originally aligned in antiparallel directions, leading to net zero polarization. Under the application of a sufficiently high electric field, the material transforms into FE phase where parallel dipoles are aligned in the direction close to the direction of the externally applied electric field, giving rise to a sharp jump in polarization. As a result, the charges are accumulated on the conductive plates, which is called the charging process, and the energy stored can be calculated by integrating the area between the charging curve and the polarization axis (the sum of the blue and green areas in Figure. 1). This stored energy can be instantly released over a very short period of time, even in nanoseconds, when needed. 14 This process is called discharging. The area between the charging and discharging curves is known as energy loss (W<sub>loss</sub>), represented by the blue area. The green area represents the recoverable energy storage. The mathematical expressions of  $W_{st}$ ,  $W_{rec}$  and efficiency ( $\eta$ ) are described as follows based on Figure 1:

Department of Chemistry and 4D LABS, Simon Fraser University, Burnaby, British Columbia, V5A 1S6, Canada. Email: zye@sfu.ca

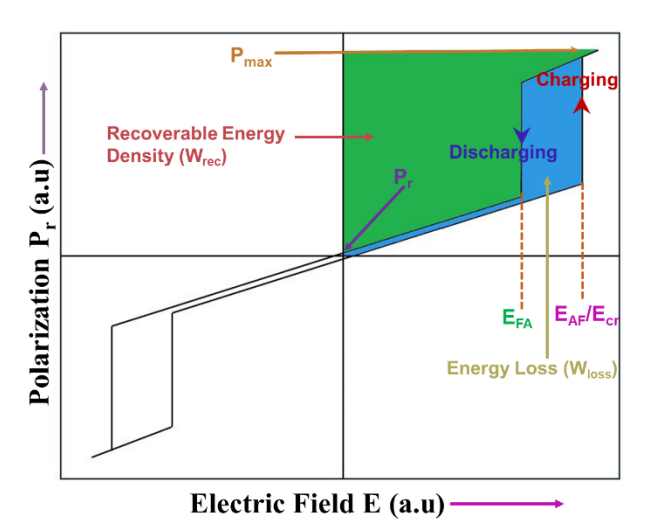


Figure. 1. Schematic of characteristic polarization-electric field (P-E) hysteresis loop used for the calculation of energy storage density. For AFEs the recoverable energy density is determined from the area in green, whereas the stored energy density is calculated by adding the area of both green and blue. The area in blue represents the unreleased energy between charging and discharging.

$$W_{st} = \int_0^{P_{max}} E dP \qquad (0 < E < E_{max}), \qquad (1)$$

$$W_{rec} = -\int_{P_{max}}^{P_r} EdP < W_{st}, \tag{2}$$

$$\eta = \frac{w_{rec}}{w_{st}} = \frac{w_{rec}}{w_{rec} + w_{loss}} \times 100 \%.$$
(3)

To increase the recoverable energy storage density, three important approaches have been taken: i) to enhance the critical electric field (Ecr) (which is required to induce the antiferroelectric to ferroelectric phase transition); ii) to enhance the dielectric breakdown strength (DBS), and iii) to increase the maximum polarization ( $P_{max}$ ). <sup>10,15-18</sup> High  $E_{cr}$  and DBS are required for those ceramics which can be used at very high applied electric fields (≥ 250 kV/cm). In contrast, the demand for high energy density dielectrics at low operating voltages is increasing ever faster, especially in the sectors of aerospace and automobile. 19 Application of a high electric field requires extraordinary supporting insulation and power systems. For this reason, dielectrics with a high energy storage density under a low or moderate applied electric field (< 230 kV/cm) are highly desirable for miniaturized and portable devices with a high degree of integration. <sup>20-21</sup> Consequently, to achieve high energy density at low operating voltages, the materials designing strategies should focus on i) low E<sub>cr</sub> and ii) high P<sub>max</sub>. The most adopted strategy to increase the energy storage density is by chemical modifications of the currently available AFE materials, which are achieved by elemental substitution or doping (either in a stoichiometric or nonstoichiometric ratio) on the A or B-site, or co-substitution/doping on both A- and B-sites of the perovskite structure, with such elements as La<sup>3+</sup>, Ti<sup>4+</sup>, Sn<sup>3+</sup>, Ta<sup>5+</sup>, Gd<sup>3+</sup>, etc., giving rise to a large number of AFE solid solutions. 17,22-30

This technique has been widely adopted in the  $Pb(Zr,Ti)O_3$  (PZT)-based antiferroelectric systems. Specifically, doping of La and Sn can help stabilize the AFE phase, and the energy storage density of the  $(Pb_{0.97}La_{0.02})(Zr_{0.66}Sn_{0.23}Ti_{0.11})O_3$  thin film was

found to be  $46.3 \text{ J/cm}^3$  with an efficiency of 84 %.  $^{28}$  Similarly, in PbHfO<sub>3</sub> (PH)-based systems, a high W<sub>rec</sub> of  $8.51 \text{ J/cm}^3$  was reported by Ge et al. as a result of compositional tuning, i.e. doping on both A- and B-sites with La<sup>3+</sup> and Ti<sup>4+</sup>, respectively,  $^{29}$  and the W<sub>rec</sub> was further increased to  $10.2 \text{ J/cm}^3$  with a 78.9 % efficiency by the substitution of Sn<sup>4+</sup> for Ti<sup>4+</sup>.  $^{30}$  However, a high field of 320 kV/cm needed to be applied.

Compositional tuning has proven to be efficient not only in leadbased antiferroelectric solid solutions but also in lead-free systems. In silver niobate AgNbO<sub>3</sub> (AN)-based solid solutions, doping or substitution of different elements either on the A- or B-site, or on both A- and B-sites of the perovskite structure creates cation vacancies for charge balance, hence giving rise to a high energy storage density.  $^{31}$  Li et al. obtained a  $W_{rec} = 7.01$ J/cm<sup>3</sup> in La-modified AN ceramics (Ag<sub>1-3x</sub>La<sub>x</sub>)NbO<sub>3</sub> with a 77 % efficiency, which is much higher than pure AN (i.e. 2 J/cm<sup>3</sup> with a 46 % efficiency). <sup>26,32</sup> Another strategy used to achieve high recoverable energy density is by introduction of polar nano regions (PNRs) into AFE materials to stabilize the AFE phase and to disrupt the FE long range order. This approach has been most widely used in lead-free materials. 13,33-34 In the 0.76NaNbO<sub>3</sub>- $0.24(Bi_{0.5}Na_{0.5})TiO_3$  ceramics, a  $W_{rec} = 12.2 \text{ J/cm}^3$  was realized with an efficiency of 80.2 %. 33 With the display of hysteresisfree P-E loop, a W<sub>rec</sub> of 9.5 J/cm<sup>3</sup> was obtained with a 92 % efficiency in  $(1-x)(Na_{0.5}Bi_{0.5})TiO_3-x(Sr_{0.7}Bi_{0.2})TiO_3.^{13}$ 

All the techniques described above aim to achieve high Wrec by increasing the values of both Ecr and DBS. Recently, a new concept of dipole frustration was applied by our group to the AFE-AFE systems to form a series of novel solid solutions. The PbHfO<sub>3</sub>-Pb(Mg<sub>1/2</sub>W<sub>1/2</sub>)O<sub>3</sub> (PH-PMW) solid solution was found to exhibit a high P<sub>max</sub> of 45 μC/cm<sup>2</sup> at a relatively low electric field of 155 kV/cm, leading to a W<sub>rec</sub> of 3.7 J/cm<sup>3</sup>. The studies of the solid solution of  $(1-x)PbZrO_3-xPb(Mn_{1/2}W_{1/2})O_3$  revealed that with the increase of x,  $E_{cr}$  decreases and  $P_{max}$  increases, indicating the softening of AFE order due to dipole frustration. 35 More recently, a high recoverable energy storage density of 5.03 J/cm<sup>3</sup> and a large strain of 0.60 % were obtained under a relatively low electric field of 200 kV/cm in the solid solution of PbHfO<sub>3</sub>-Pb( $Zn_{1/2}W_{1/2}$ )O<sub>3</sub> (PH-PZW). <sup>36</sup> In these three systems, the antiparallel alignment of Pb2+ in both PbZrO3 and PbHfO3 is along the  $[110]_{pc}$  direction, whereas in Pb(Mg<sub>1/2</sub>W<sub>1/2</sub>)O<sub>3</sub> and Pb(Mn<sub>1/2</sub>W<sub>1/2</sub>)O<sub>3</sub>, it is along the  $[100]_{pc}$  and  $[010]_{pc}$  directions. <sup>37</sup> These different polar arrangements lead to frustration in the dipole interaction in the subsequent solid solutions. These studies show that, it is possible to achieve high energy density at a relatively low electric field through creation of dipole frustration.

Based on the above literature analysis and observations, we propose to design and synthesize a novel AFE-ferrielectric solid solution which can display a large maximum polarization and a high energy density at a relatively low critical field. Among the typical AFE materials, lead hafnate PbHfO<sub>3</sub> (PH) has gained increasing attention thanks to its potential for energy storage applications on the one hand, and some intricate fundamental issues on the other hand, such as the nature of its intermediate phase, which possibly has an incommensurate structure. <sup>38-39</sup> PH is isostructural to PZ and shares the same space group,

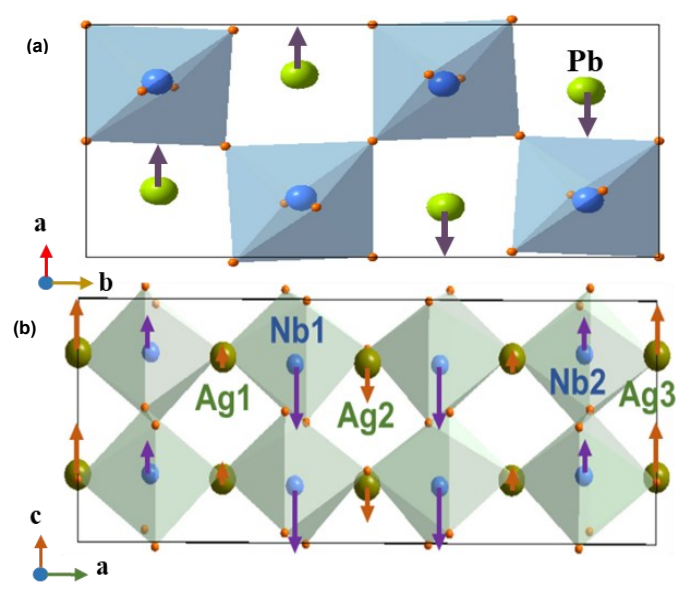


Figure 2. Refined crystal structure of (a) PbHfO $_3$  and (b) AgNbO $_3$  with the Pbam and Pmc2 $_1$  space groups, respectively. Displacements of Pb $^{2+}$  ions in PbHfO $_3$  and Ag $^+$  and Nb $^{5+}$  ions in AgNbO $_3$  along the [110] $_{pc}$  directions are represented by arrows.

Pbam, at room temperature. The antiparallel displacement of Pb<sup>2+</sup> ions along the pseudocubic [110]<sub>pc</sub> direction is responsible for the antiferroelectricity in PH. The hybridization between the Pb<sup>2+</sup> 6s and O<sup>2-</sup> 2p orbitals favours a high P<sub>max</sub>, leading to a high energy density.  $^{40}$  Recently, it was found that PbHfO<sub>3</sub> exhibits a characteristic double hysteresis loop, resulting in a W<sub>rec</sub> of 2.7 J/cm³.  $^{41}$  The intermediate phase of PH suggests an AFE nature with the Imma space group.  $^{41}$  Furthermore, chemical modifications to PH have proved to be effective in enhancing the energy storage density.  $^{18,24,29-30}$  All these qualities of PH make it a favourable AFE material as the base of new solid solution systems.

When selecting a ferrielectric end member to form the new solid solution with PH, we consider lead-free systems with an attempt to reduce the lead contents for environment and health benefits. <sup>42-44</sup> Silver niobate AgNbO<sub>3</sub> (AN)-based ceramics have proved to exhibit good energy storage capabilities. <sup>45</sup> However, the exact crystal structure of AN at room temperature

is still under debate. By careful structural analysis based on neutron powder diffraction, synchrotron powder diffraction, convergent-beam electron diffraction and selected-area electron diffraction, Yashima et al. suggested a ferrielectric (weakly ferroelectric), orthorhombic Pmc21 structure for AN at room temperature, in which Ag+ and Nb5+ exhibit antiparallel, but not fully compensated displacements along [110]<sub>pc</sub> so that a weak spontaneous polarization appears in this direction. 46 From crystal chemistry point of view, AN suffers from serious drawbacks. For instance, due to the thermodynamic instability of Ag<sup>+</sup> ions at high temperatures, it is difficult to synthesize pure AN via conventional solid-state reaction route without the presence of an oxygen-enriched atmosphere. 47 To overcome these issues, we propose to prepare a novel solid solution between AFE PH and weakly ferroelectric (or ferrielectric) AN, with varying concentration of AN. As shown in Figure 2-(a, b), the antiparallel alignments of Pb2+ in PbHfO3 and Ag+ and Nb5+ in AgNbO<sub>3</sub> are along the [110]<sub>pc</sub> direction but with different magnitudes for Ag<sup>+</sup> and Nb<sup>5+</sup>. Therefore, formation of the PH-AN solid solution is expected to induce an incommensurate modulation <sup>48</sup>. It is also expected that a small amount of AN can be stabilized in the PH-AN solid solution without the use of an oxygen-enriched atmosphere. The concept, approaches and goal in the design and preparation of the solid solution between antiferroelectric PH and ferrielectric AN is illustrated in Figure 3. Accordingly, the solid solution of (1-x)PbHfO<sub>3</sub>-xAgNbO<sub>3</sub> is synthesized and investigated to achieve low  $E_{\text{cr}}\text{, high }P_{\text{max}}$  and high  $W_{rec}$ . A significantly high  $W_{rec}$  of 4.8 J/cm<sup>3</sup> is achieved for x = 0.027 with a  $P_{max}$  of 55  $\mu C/cm^2$  at an applied field of 172 kV/cm, which is remarkably higher than all the known solid solutions at a similar applied field.

# 2. Experimental

#### 2.1. Materials preparation

The solid solutions (1-x)PbHfO<sub>3</sub>-xAgNbO<sub>3</sub> (x = 0.01, 0.02, 0.025, 0.027, 0.03 and 0.04) were prepared in the form of ceramics by a cost-effective conventional solid state reaction route. Reagent

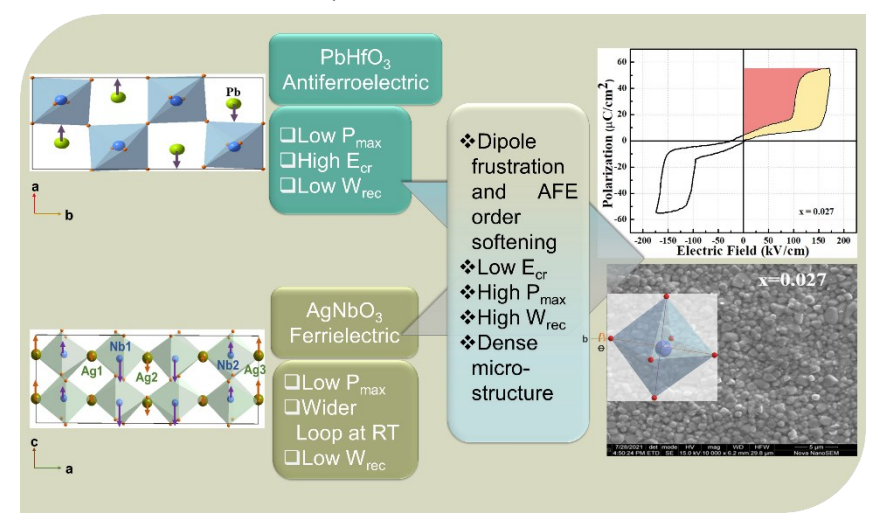


Figure 3. Schematic diagram illustrating the concept, approaches and goal in the design and preparation of a new solid solution system between antiferroelectric PH and ferrielectric AN, (1-x)PbHfO<sub>3</sub>-xAgNbO<sub>3</sub>, with enhanced maximum polarization and recoverable energy storage density at low operating fields.

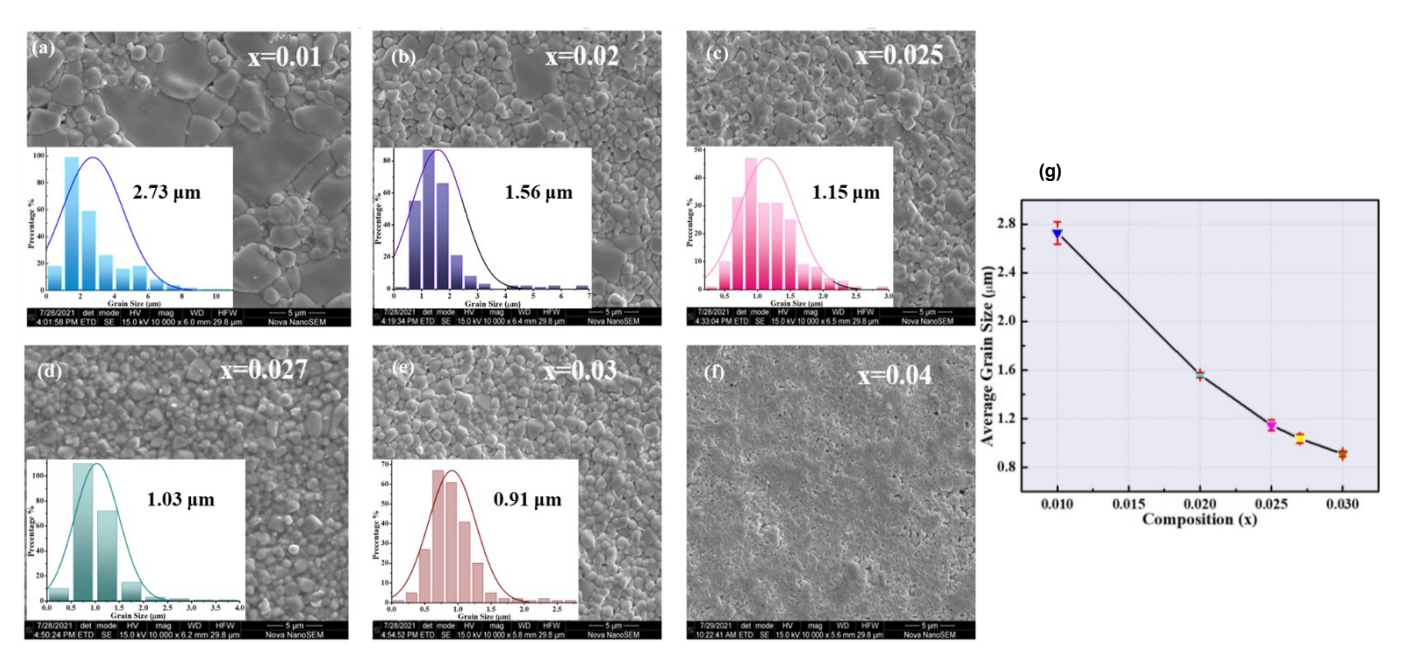


Figure 4. (a-f) SEM images of the surfaces of as-sintered  $(1-x)PbHfO_3$ - $xAgNbO_3$  (x = 0.01, 0.02, 0.025, 0.027, 0.03 and 0 .04) ceramics, with the grain size distribution and average grain size represented in Insets. (g) Variation of the average grain size as a function of AgNbO<sub>3</sub> concentration, with error bars presented by red colour.

grade oxides of PbO (Alfa Aesar, 99.9 %), HfO2 (Aldrich Chemistry, 98 %), Ag<sub>2</sub>O (Alfa Aesar, 99 %), Nb<sub>2</sub>O<sub>5</sub> (STREM Chemicals, 99.9 %) were used as starting materials which were weighed and mixed according to the stoichiometric ratios. The powders were thoroughly mixed and hand ground for two hours in the presence of an ethanol medium. The slurry was then dried at room temperature and pressed into pellets of 20 mm in diameter under a pressure of 300 MPa. The pressed pellets were calcined at 900 °C for 6 hrs. To prevent or minimize the volatilisation of PbO at high temperatures, a double crucible method was used. In this process, the pellets were placed on an alumina plate. This plate was then covered with a smaller alumina crucible whose diameter is large enough to cover all the pellets. An extra PbO powder was placed on top of the smaller alumina crucible. The smaller crucible with the pellets inside was then covered with another  $Al_2O_3$  crucible of larger diameter so that a high partial pressure of PbO was maintained during calcination. The calcined pellets were then crushed, hand ground for two hours and mixed with 5 % PVA for better binding. The PVA-mixed powder was again pressed into pellets with a diameter of 10 mm and a thickness of 1 mm. The pellets were then sintered at 1100 °C for 4 hrs to obtain highly dense ceramics. To prevent or compensate the volatilization of PbO during sintering, the pellets were submerged into a sacrificial powder of the respective composition. The obtained ceramics were light yellow in colour. It is believed that the density of the (1-x)PbHfO<sub>3</sub>-xAgNbO<sub>3</sub> ceramics could be further improved, and their properties optimized, using a ball milling process, especially in scaled-up production of the materials for potential applications. To perform the study of electrical properties, the sintered ceramics were polished to obtain smooth and parallel circular faces. Silver paste was applied on the circular faces of the ceramics as electrodes and fired at 550 °C for 30 min. to form good Ohmic contacts.

#### 2.2 Characterizations

The phases and crystal structures of the as-sintered ceramics were examined and analysed using a high-resolution X-ray diffractometer (Bruker, D8 Advance diffractometer with copper  $K\alpha_1$  tube). The microstructure of the as-sintered pellets was investigated by scanning electron microscopy (Novo NanoSEM 430). The temperature dependence of permittivity was measured from room temperature to 400 °C using a Novocontrol Alpha high-resolution broadband dielectric spectrometer equipped with a temperature-controlled Novotherm HT furnace over the frequency range of 100 Hz to 1 MHz. The samples used to measure the dielectric properties had a thickness of approximately 0.8 mm. The polarization-electric field (P-E) hysteresis loops were measured on ceramic samples of a thickness of 0.12 ± 0.05 mm using a ferroelectric analyser (Radiant RT66A Standard Ferroelectric Testing System) at 10 Hz at ambient temperature. At high temperatures, the P-E loops were measured using a DELTA 9023 furnace.

# 3. Results and Discussion

### 3.1 Microstructures analysis

Figure 4-(a-f) shows the microstructure and surface morphology of the as-sintered (1-x)PbHfO<sub>3</sub>-xAgNbO<sub>3</sub> ceramics with various compositions. All the ceramics exhibit clear grain boundaries and close-packed grains with minimal porosity. The insets of Figure 4-(a-e) show the grain size distribution and the average grain size of each composition, which were calculated with the help of IMAGEJ software. For x = 0.04, the size of the grains was so small that it is difficult to obtain meaningful grain size distribution and average grain size (Figure. 4-(f)). For each sample, more than 200 points were taken into consideration. It can be seen from Figure 4-(g) that, with the increase in the concentration of Ag<sup>+</sup> and Nb<sup>5+</sup> substituting on the A- and B-sites,

respectively, the average grain size decreases significantly from  $^\sim 2.7~\mu m~(x=0.01)$  to  $^\sim 0.91~\mu m~(x=0.03)$ . This suggests that the substitution of AgNbO3 inhibits the grain growth. Small grain size and dense microstructure usually lead to high dielectric breakdown strength (DBS) values of the ceramics, which is considered as one of the important factors in increasing the energy storage density in many cases.  $^{26,30\text{-}31}$  The relative density of all the ceramics with AN substitution up to x = 0.03 is found to be  $\geq 95~\%$  of the theoretical density. It decreases to 89 % for x = 0.04.

#### 3.2 Dielectric Properties and Phase Transitions

Figure 5-(a-e) displays the temperature and frequency dependences of the relative permittivity of the as-sintered (1x)PbHfO<sub>3</sub>-xAgNbO<sub>3</sub> ceramics (the room temperature variation of relative permittivity is presented in Figure S.1 (a-e)). It is well known that the permittivity of PH shows two sharp anomalies when measured as a function of temperature. The peak at the higher temperature ( $T_{C2}$  = 199 °C) corresponds to the phase transition from the paraelectric (PE) cubic, Pm3m phase to the AFE, orthorhombic, Imma symmetry (AFE2) upon cooling, while the step at the lower temperature ( $T_{C1} = 163 \, ^{\circ}\text{C}$ ) represents the phase transition from AFE<sub>2</sub> to another AFE, orthorhombic Pbam phase (AFE<sub>1</sub>).  $^{43,49}$ . Similar behaviour is observed for x = 0.01. For compositions between x = 0.02 and x = 0.03, an additional weak dielectric anomaly appears in between the AFE2 and PE phases, giving rise to an intermediate phase (IM) which is found to be an orthorhombic Imma phase. The details of this phase will be

discussed in the following Sections. With the increase in the AN concentration, the phase transition temperature  $T_{CI}$  decreases from 138 °C (x = 0.01) to 95 °C (x = 0.03). Since  $T_{CI}$  is far above the room temperature, the samples remain in the AFE<sub>1</sub> state at room temperature.

Meanwhile, the phase transition temperature between the AFE<sub>2</sub> and IM phase slightly decreases from 190 °C to 179 °C for the compositions of  $0.02 \le x \le 0.03$ . Furthermore, the temperature of the permittivity peak at  $T_{C1}$  decreases as the concentration of AN increases to  $x \le 0.03$ .

To examine the reversibility of the AFE<sub>1</sub>, IM and AFE<sub>2</sub> phases and phase transitions, the temperature dependent dielectric response was measured upon heating and cooling. The heating and cooling curves for x = 0.01, x = 0.025 and x = 0.027 are presented in Figure 5-(f-h), respectively. A significant thermal hysteresis of the AFE<sub>1</sub> – AFE<sub>2</sub> phase transition is found for all the compositions, which signifies that this phase transition is of first order. Moreover, it is found that with the increase in the concentration of AN, the thermal hysteresis also increases, indicating that the first-order characterstic becomes more obvious. On the other hand, the AFE<sub>2</sub> – PE (for x = 0.01) phase transition, and the AFE<sub>2</sub> – IM and IM – PE (x = 0.027) phase transitions only show a slight thermal hysteresis, suggesting a weak first order nature. The temperature dependensies of loss tangent and imaginary part of permittivity of the as-sintered (1x)PbHfO<sub>3</sub>-xAgNbO<sub>3</sub> ceramics are presented in Figure S.2 and S.3, respectively.

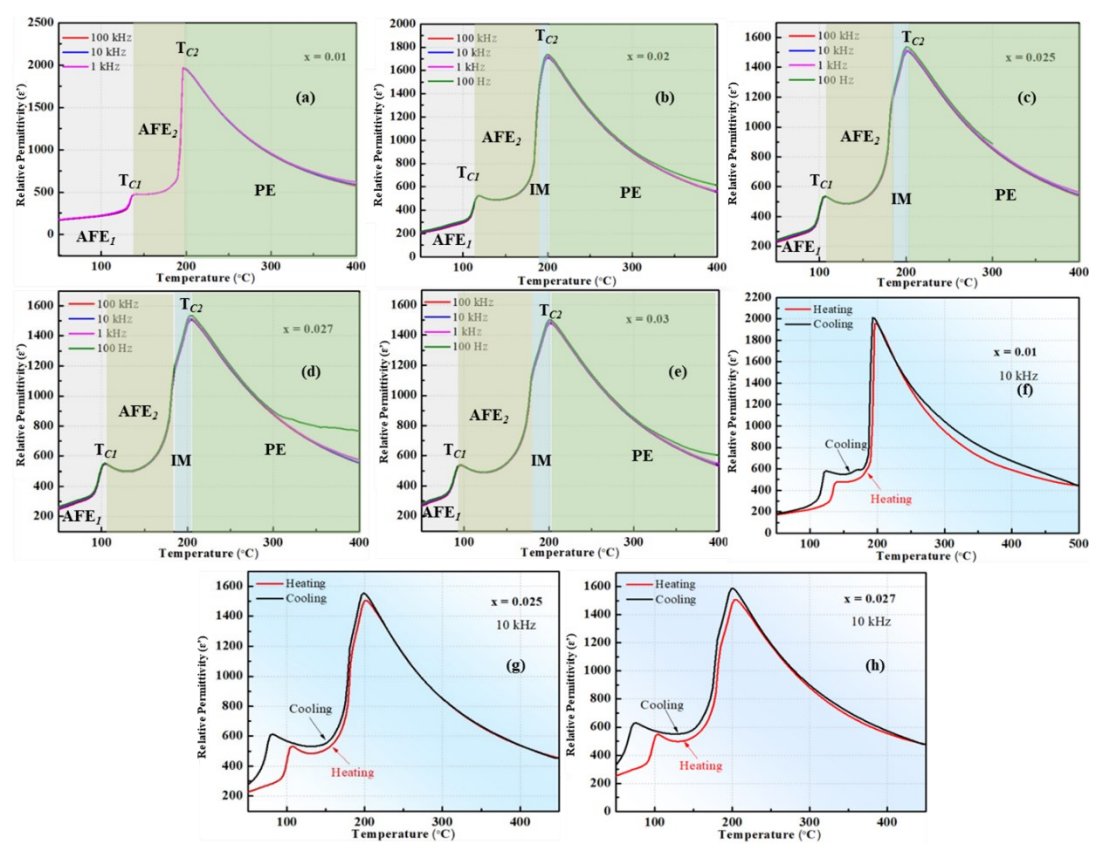


Figure 5. (a-f) Variation of dielectric constant as a function of temperature for various compositions of the (1-x)PbHfO<sub>3</sub>-xAgNbO<sub>3</sub> ceramics. The data were measured at various frequencies upon cooling. Variation of dielectric constant as a function of temperature for (f) x = 0.01, (g) x = 0.025 and (h) x = 0.027, measured upon heating and cooling at 10 kHz.

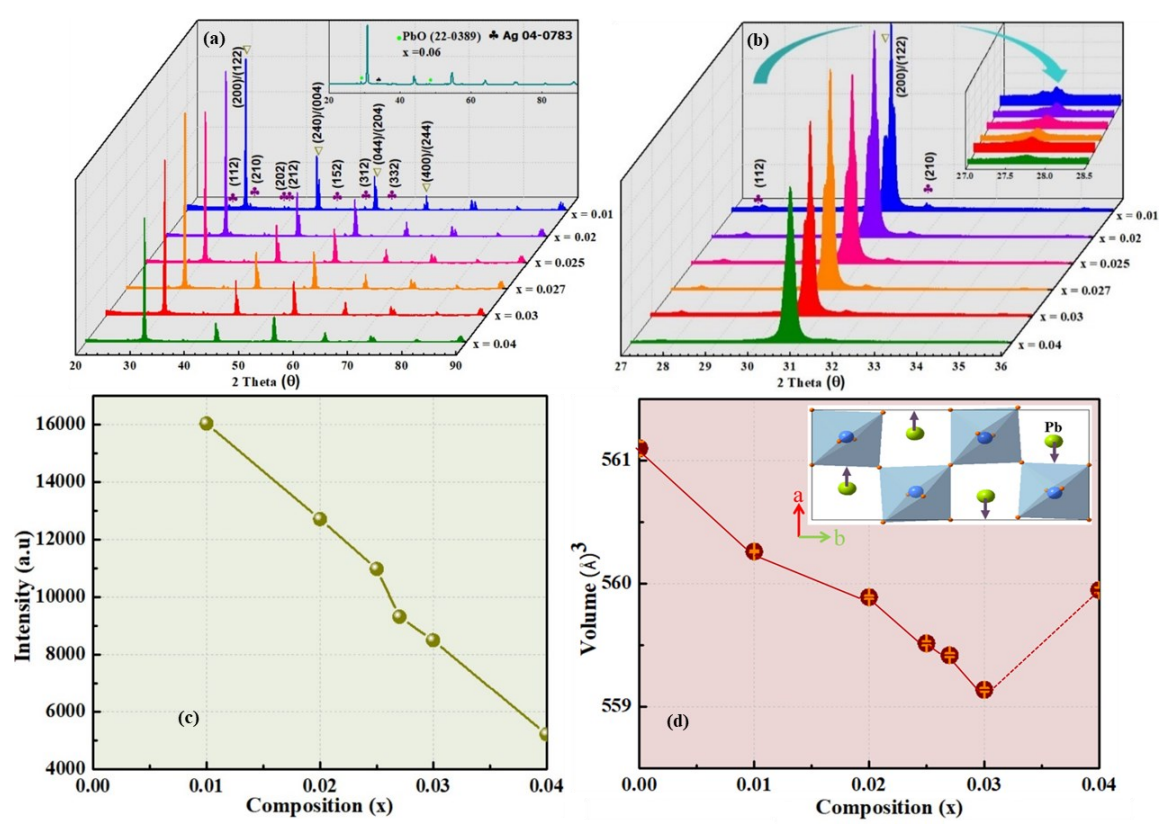


Figure 6. (a) XRD patterns of the solid solution  $(1-x)PbHfO_3$ -xAgNbO $_3$  with different compositions measured at room temperature. The peaks are labelled according to the orthorhombic setting. Inset shows that XRD pattern of composition x = 0.06 with marked trace impurities of PbO and Ag. (b) Enlarged view of the peaks between  $2\Theta = 27$  to  $30^\circ$ , where the ½ superlattice reflections and simple perovskite peaks were marked by " $\P$ " and " $\nabla$ ", respectively. Inset shows the enlarged ½ superlattice peaks at  $27.7^\circ$ . (c) Variation of the intensity of ½ superlattice peak with composition. (d) Variation of the unit cell volume as a function of concentration x with the corresponding crystal structural model for x = 0.02, with error bars presented by orange colour.

# 3.3 Structural analysis

Figure 6-(a-b) shows the room temperature XRD patterns of the (1-x)PbHfO<sub>3</sub>-xAgNbO<sub>3</sub> ceramics with various compositions. All

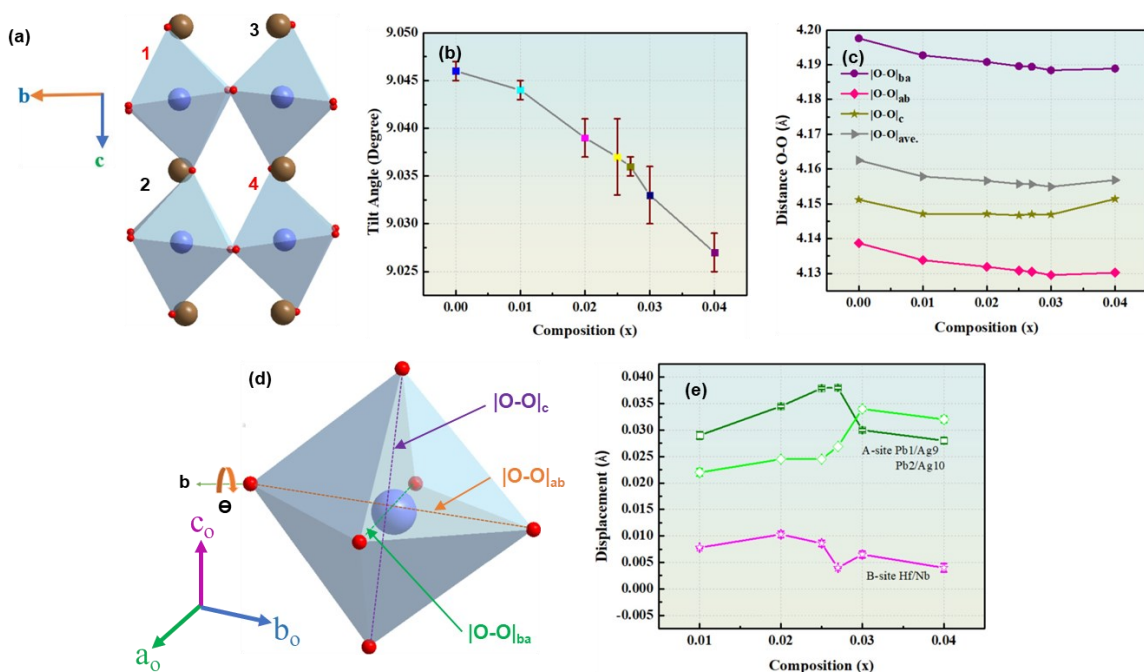


Figure 7. (a) Arrangements of  $[B0_6]$  octahedra with the (a a c 0) tilting assigned according to the Glazer notation. <sup>52</sup> (b) Variation of the tilting angle (ø) as a function of composition x of the (1-x)PbHfO<sub>3</sub>-xAgNbO<sub>3</sub> solid solution, with error bars presented in wine colour. (c) Illustration of the distances between two oxygens along the  $|O-O|_{ab}$ ,  $|O-O|_{ba}$  and  $|O-O|_{c}$  directions of a  $|BO_6|$  octahedron from which the average distances between  $|O-O|_{ave}$  are calculated. (d)  $|BO_6|$  octahedron following the a a c 0 tilt (where,  $a_0 = \sqrt{2}a_{pc}$ ,  $b_0 = 2\sqrt{2}a_{pc}$ ,  $c_0 = 2a_{pc}$ ). (e) Displacements of the A-site (Pb<sup>2+</sup>/Ag<sup>+</sup>) and B-site (Hf<sup>4+</sup>/Nb<sup>5+</sup>) cations as a function of x, with error bars presented in dark green, light green and pink colours, respectively.

the prepared samples crystallize in the perovskite structure, and no secondary phase is found till x = 0.04, indicating that the Ag<sup>1+</sup> and Nb5+ cations are well incorporated into the lattice sites of the Pb<sup>2+</sup> and Hf<sup>4+</sup> cations, respectively. All the perovskite peaks are marked with " $\nabla$ ". The low intensity peaks marked with " $\Phi$ " are identified as the ¼ superlattice peaks, which are associated with the antiparallel arrangement of Pb2+ cations along the  $[110]_{pc}$  directions,  $^{49-51}$  characteristic of the PH structure. For higher concentrations of AN (x  $\geq$  0.04), secondary phases related to the PbO and Ag trace impurities (PDF 22-0389 and 04-0783) are observed, which indicates that the solubility of AN in PH has been exceeded (Inset, Figure 6-(a)). All the observed diffraction peaks can be indexed with the orthorhombic Pbam (PDF 27-1191) symmetry. For a better visualization of the superlattice, the orthorhombic  $V2a_{pc}\times\,2V2a_{pc}\,\times\,2a_{pc}$  lattice setting is converted into a pseudocubic lattice setting, as mentioned in our previous paper. 41

In order to analyse the detailed crystal structure of the  $(1-x)PbHfO_3$ -xAgNbO $_3$  ceramics, an enlarged view of the superlattice ((112)/(210)) peaks and the simple perovskite ((200)/(122)) peaks are presented in Figure 6-(b). No obvious change is noticed in the shape of the perovskite ((200)/(122)) peak, which splits for  $x \le 0.03$ . For x > 0.03, a single peak is observed, indicating that all the compositions with  $x \le 0.04$  are in the orthorhombic Pbam phase. As the concentration of AN increases, the intensity of the  $\frac{1}{2}$  superlattice peaks decreases (Figure 6-(c)). This suggests that the magnitude of the antiparallel displacement of A-site ions becomes smaller.

Figure 6-(d) depicts the variation of the unit cell volume as a function of AN concentration. It can be clearly seen that the cell volume decreases systematically till x = 0.03, which can be attributed to the fact that the ionic radii of  $Ag^{+1}$  (1.28 Å) and  $Nb^{5+}$  (0.74 Å) are smaller than the ionic radii of  $Pb^{+2}$  (1.49 Å) and  $Hf^{+4}$  (0.97 Å). However, for x = 0.04, the volume of the unit cell

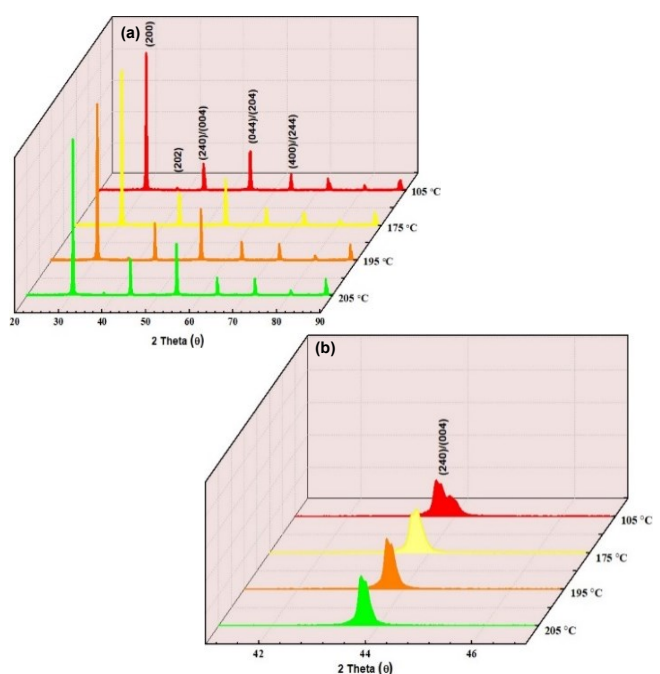


Figure 8. (a) XRD patterns of the  $0.973PbHfO_3$ - $0.027AgNbO_3$  ceramics measured at different temperatures. (b) Enlarged view of the (240)/(004) peaks around  $2\Theta = 44^{\circ}$ .

increases significantly. It may be possible that the solid solution of  $(1-x)PbHfO_3$ -xAgNbO $_3$  reaches the morphotropic phase boundary at x  $^{\sim}$  0.04, but it is difficult to resolve the symmetry of the MPB phase(s) from X-ray diffraction patterns.

The structural characteristics are also examined with the Rietveld refinement and the results are presented in Figure 7-(a-e). Figure 7-(a) presents the average shape and arrangement of the [BO<sub>6</sub>] octahedron. It is clearly visible that 1 and 4 [BO<sub>6</sub>] octahedrons are tilted out of phase, whereas 3 and 2 are tilted in phase, which originates from the antiparallel arrangement of the dipoles. This tilting of octahedrons can be assigned to the (a-a-c<sup>0</sup>) type according to the Glazer notation. <sup>52</sup> A systematic decrease in the value of octahedral tilting angle (ø) with the increase of AN content is observed in Figure 7-(b). Moreover, the distances between two oxygens of a [BO<sub>6</sub>] octahedron along the ab ( $|O-O|_{ab}$ ), ba ( $|O-O|_{ba}$ ) and c ( $|O-O|_c$ ) directions and the average length ( $|O-O|_{ave.}$ ) between them also decrease till x  $\leq$ 0.03 (Figure 7-(c-d)). However, for x = 0.04 the |O-O| length slightly increases, which is consistent with the lattice parameters obtained from the Rietveld refinement. The decrease in the |O-O|ave. and tilting angles (ø) values for the compositions with x less than 0.03 cause compression in the octahedron due to chemical pressure arising from the substitutions (Ag+ for Pb2+, and Nb5+ for Hf4+). 16 Figure 7-(e) shows the A- and B-site cation displacements from their ideal positions. On average, the displacement of the A-site cation increases till x = 0.027, but for higher concentrations of AN  $(0.027 \le x \le 0.04)$ , it shows a decreasing trend. Conversely, the displacement of B-site cation decreases slightly for all the concentrations. Thus, an optimal substitution of Ag+ for Pb2+ increases the off-centring of A-site cations with respect to the oxygen octahedrons.

To determine the structure of the high-temperature phases observed in the dielectric studies for the compositions of  $0.02 \le x \le 0.03$ , a detailed temperature-variable structural analysis was carried out for x = 0.027 by the Rietveld refinements using the GSAS software. <sup>53</sup> For x = 0.027, the intermediate (IM) phase lies

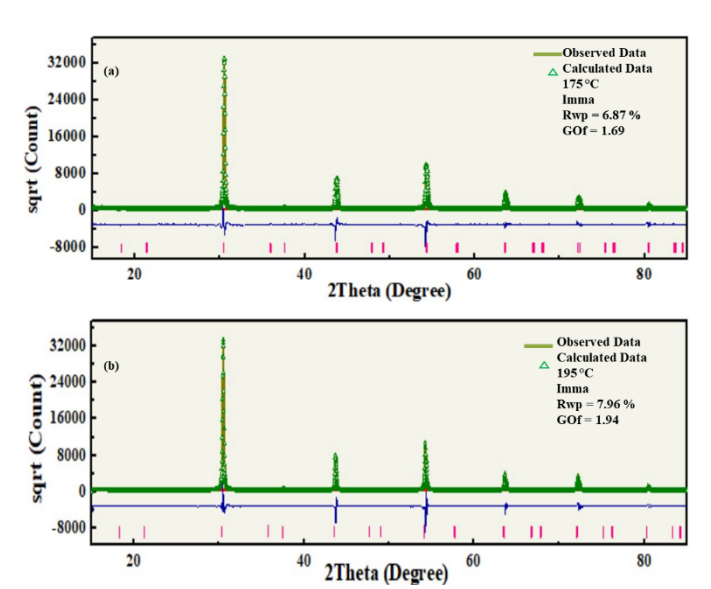


Figure 9. Rietveld refinement results of the  $0.973PbHfO_3$ - $0.027AgNbO_3$  ceramics measured at (a) 175 and (b) 195 °C.

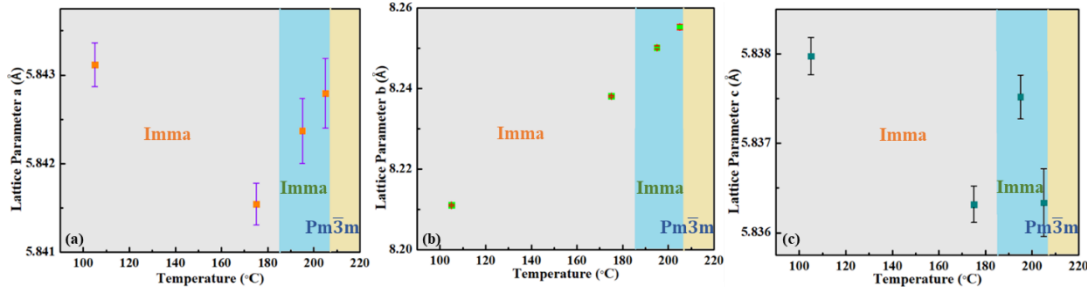


Figure 10. Variations of lattice parameters a (a), b (b) and c (c) of the 0.973PbHfO<sub>3</sub>-0.027AgNbO<sub>3</sub> solid solution measured at temperatures between 105 to 205 °C, with error bars presented in purple, orange and grey colours, respectively.

within a very narrow temperature range from 185 to 203 °C. Figure 8-(a) depicts the XRD patterns for x = 0.027 which were measured at temperatures between 105 and 205 °C. No evidence of superlattice peaks is found in this temperature range. The enlarged view of the (240)/(004) peaks in Figure 8-(b) reveals a reduction in peak splitting upon heating. However, no significant changes are observed upon entering the IM phase at 185 °C, suggesting that the symmetry of the IM phase may be similar to that of the AFE2 phase. This conclusion is further supported by the Rietveld refinement results, which are presented in Figure 9-(a-b). A good agreement between the calculated and observed data is clearly evidenced. As discussed earlier, the room temperature XRD pattern fits well to the orthorhombic Pbam symmetry. Since no superlattice peaks are found at high temperatures, the Pbam space group can be

excluded. Therefore, the orthorhombic Imma space group is chosen as a model to carry out the structural fitting of the XRD data for the AFE<sub>2</sub> structure (105 and 175 °C), which was proposed by Bosak et al.<sup>39</sup> Low values of the reliability factor of weighted patterns ( $R_{wp}$ ) and the goodness of fit (GOF) are obtained, as presented in Figure 9-(a), which indicate the correctness of the Imma structure for the AFE<sub>2</sub> phase in the given temperature range. However, further studies with synchrotron X-ray and/or neutron diffraction would be needed to confirm the Imma space group for the IM phase. We performed several fittings using the different models (Figure S.4. (a-c)), but Imma is the best fit model for IM phase too (195 and 205 °C) (Figure 9-(b)), with low values of  $R_{wp}$ , GOF and weak residuals. The refined structural parameters are presented in Table S.1. Figure 10-(a-c) presents the lattice parameter

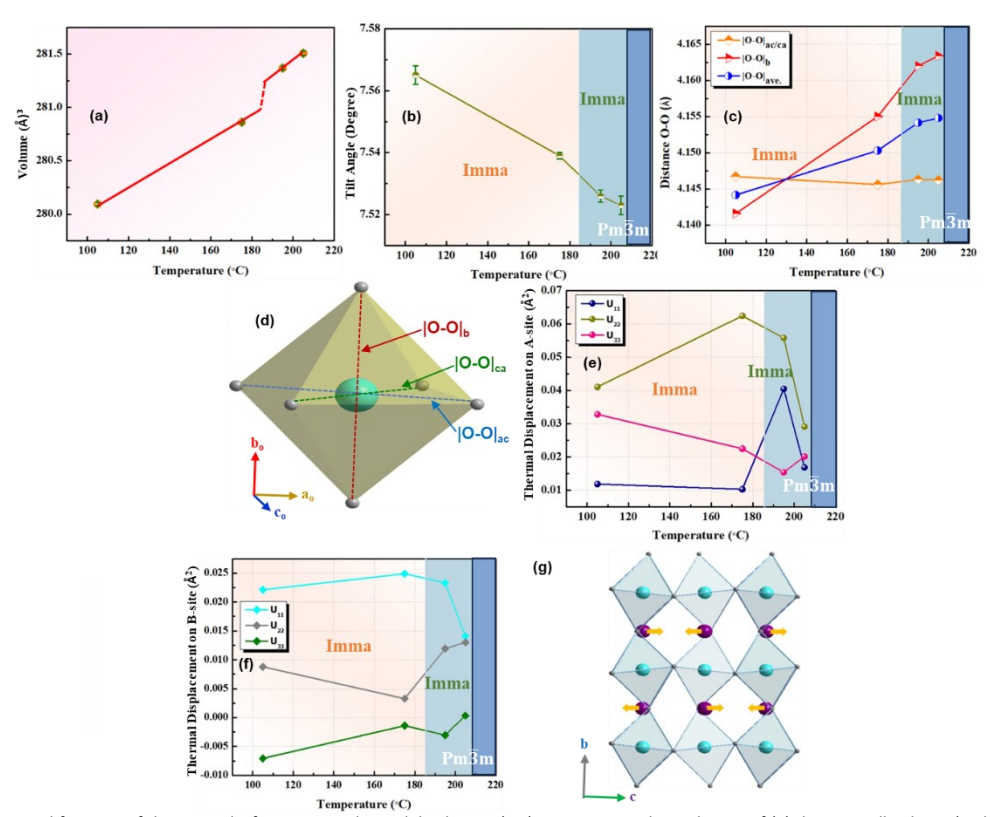


Figure 11. Refined structural features of the  $0.973PbHfO_3$ - $0.027AgNbO_3$  solid solution. (a-c) Temperature dependences of (a) the unit cell volume (with error bars presented in green colour), (b) the tilting angle of the octahron of the (a-a-c<sup>0</sup>) type (with error bars presented in dark green colour) and (c) distances between the two oxygens along the a ( $|O-O|_{ac/ca}$ ) and b ( $|O-O|_{b}$ ) directions, and average distance between O-O ( $|O-O|_{ave.}$ ). (d) [BO<sub>6</sub>] octahedron following the a-a-c<sup>0</sup> tilt (where,  $a_o = V2a_{pcr.}$   $b_o = 2V2a_{pcr.}$   $c_o = 2a_{pc}$ ). (e-f) Variations of the thermal displacements of A-site (Pb<sup>2+</sup>/Ag<sup>+</sup>) (e) and B-site (Hf<sup>4+</sup>/Nb<sup>5+</sup>) (f) cations as a function of temperature. The area shaded in light blue represents the region of the IM phase. (g) Refined crystal structures of  $0.973PbHfO_3$ - $0.027AgNbO_3$  at 175 °C (AFE<sub>2</sub>) with the Imma space group. Light blue polyhedrons stand for the [Hf<sup>4+</sup>/Nb<sup>5+</sup>O<sub>6</sub>] octahedrons. Purple and blue spheres represent the A (Pb<sup>2+</sup>/Ag<sup>+</sup>) and B (Hf<sup>4+</sup>/Nb<sup>5+</sup>) cations, respectively.

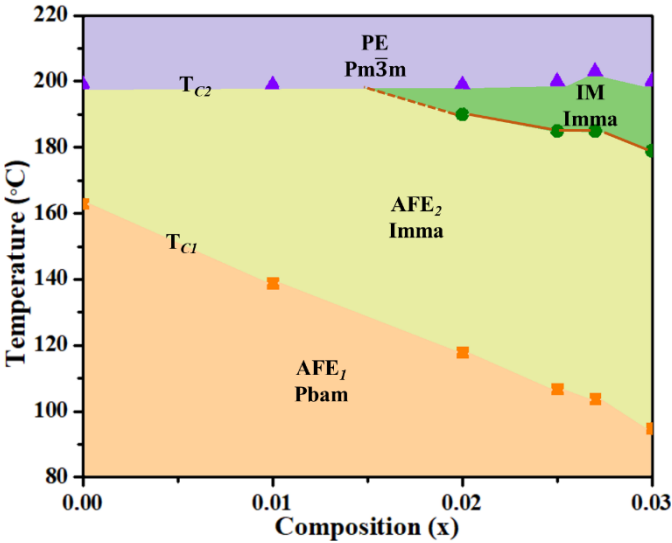


Figure 12. Phase diagram for the (1-x)PbHfO<sub>3</sub>-xAgNbO<sub>3</sub> (0 $\le x \le 0.03$ ) solid solution in terms of temperature and composition x, which delimits the various phase areas including the AFE<sub>7</sub>, AFE<sub>7</sub>, IM and PE phases, the transformation between them.

variation for x = 0.027 measured at temperatures between 105 to 205 °C. The sudden increase in lattice parameter a and c while entering the IM phase (Figure 10-(a) and (c)) supports the phase transition from the AFE<sub>2</sub> orthorhombic Imma phase to another orthorhombic IM phase of the Imma space group. With the increase in temperature, the unit cell volume increases as a result of thermal expansion (Figure. 11-(a)).

To analyse the structure of high temperature phase in more detail, the characteristic structural parameters obtained from the refinements are studied. As shown in Figure 11-(b), with the increase in temperature, the tilting angle ( $\emptyset$ ) of [BO<sub>6</sub>] octahedron, (which follows the a-a-c<sup>0</sup> tilting scheme according to the Glazer notation) decreases. The lengths between the two oxygen ions in the octahedron on the ac/ca-axis remain almost

unchanged with increasing temperature, while the  $|O-O|_b$  length on the b-axis increases. Overall, the trend of the average  $|O-O|_{ave.}$  distance increases (Figure 11-(c)), because with the rise in temperature, the oxygen octahedron expands. Note that the variations of the tilting angle of  $[BO_6]$  and the |O-O| length show a smaller change in slope in the temperature range of 185 to 205 °C (IM phase) (represented by light blue-shaded area in Figure 11-(b-c)) in comparison to the slope in the Pbam phase. This observation supports the phase transition from the AFE $_2$  orthorhombic Imma phase to another orthorhombic IM phase of the Imma space group. Further evidence of the phase transition is provided by the sharp changes found in the thermal parameters  $U_{11}$ ,  $U_{22}$  and  $U_{33}$  around the AFE $_2$  to IM phase transition, as shown in Figure 11-(e-f). To reveal the direction of

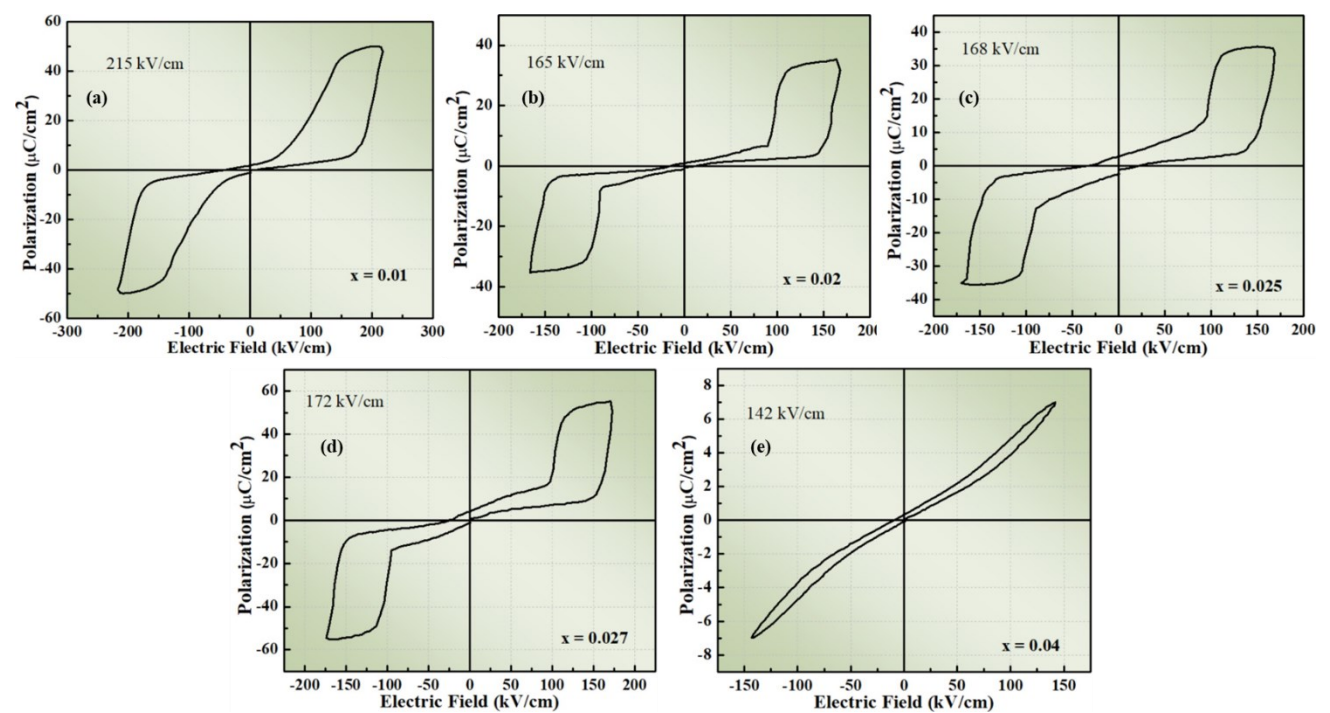


Figure 13. Polarization-electric field (P-E) relations of the (1-x)PbHfO<sub>3</sub>-xAgNbO<sub>3</sub> ceramics with x = 0.01 (a), 0.02 (b), 0.025 (c), 0.027 (d) and 0.04 (e), at ambient temperature.

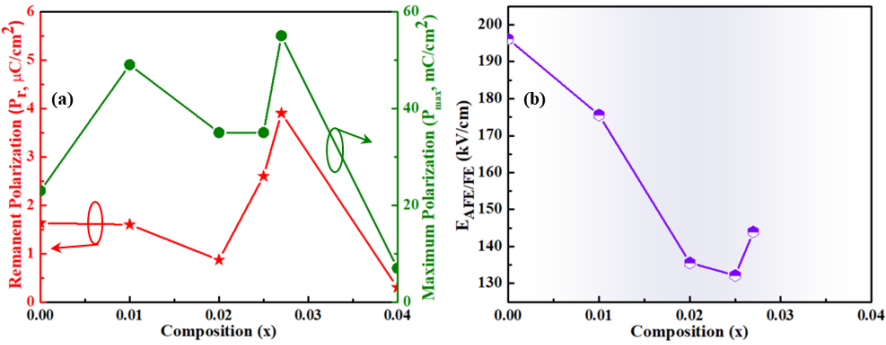


Figure 14. (a) Variations of the remanent polarization ( $P_r$ ) and maximum polarization ( $P_{max}$ ) as a function of composition for the (1-x)PbHfO<sub>3</sub>-xAgNbO<sub>3</sub> solid solution. (b) Variation of the critical electric field ( $E_{cr}$ ) as a function of composition x.

the antiparallel alignment of A-site cation, the refined crystal structure for 175 °C is constructed with the help of DIAMOND 4 software (Figure 11-(g)). Interestingly, it is found that the alignments of the A-site cations (Pb<sup>2+</sup>/Ag<sup>+</sup>) in both the AFE<sub>2</sub> and IM phases are along the [001]<sub>pc</sub> axis, as presented in Figure 11-(g).

Based on the above results, analysis and discussion, a (partial) phase diagram of the (1-x)PH-xAN solid solution is established in terms of temperature and composition, as depicted in Figure 12.

#### 3.4 Energy storage performance

In order to evaluate the influence of the substitutions of heterovalent cations, i.e. Ag<sup>+</sup> for Pb<sup>2+</sup> on the A-site and Nb<sup>5+</sup> for Hf<sup>4+</sup> on the B-site, on the energy storage performance, the relationships between polarization and external electric field (P-E loops) were characterized in detail. The P-E loops for the (1-x)PbHfO<sub>3</sub>-xAgNbO<sub>3</sub> ceramics were measured at room

temperature, 10 Hz frequency, with the maximum field applied which is approximately equal to the dielectric breakdown strengths. The P-E loops are shown in Figure 13-(a-e). All the loops exhibit a typical AFE behaviour, which confirms that all the samples are in the AFE<sub>1</sub> phase. For  $x \le 0.03$ , the values of  $P_{max}$ are between 35 and 55 μC/cm<sup>2</sup>, which are significantly higher than the reported value for PH (23  $\mu$ C/cm<sup>2</sup>). This enhancement of P<sub>max</sub> due to the electric-field-induced AFE-FE phase transition is expected to lead to a large energy density. Non-monotonic variations are observed for the values of  $P_{\text{max}}$  and  $P_{\text{r}}$  as the function of the concentration of AN, as shown in Figure 14-(a). It is interesting to note that the highest  $P_{max}$  of 55  $\mu$ C/cm<sup>2</sup> is observed for x = 0.027, which is associated with the largest displacement of the A-site cation in the AFE phase. The value of remanent polarization increases with the increasing concentration of AN up to x = 0.027. At the same time, a decrease in the value of Ecr is noticed, as plotted in Figure. 14-(b), which is probably due to dipole frustration. A change in the

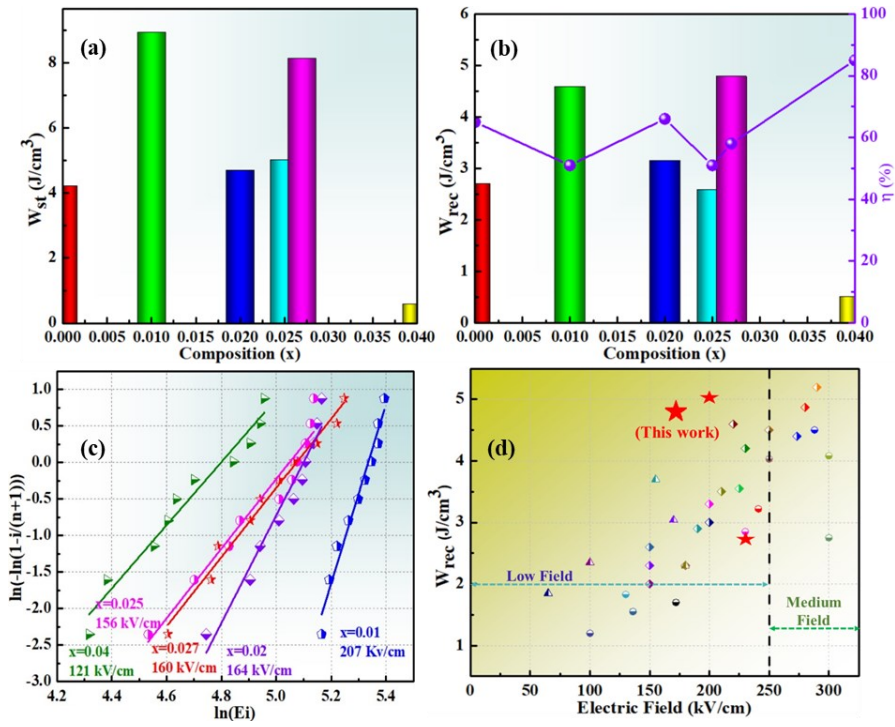


Figure 15. (a-b) Stored energy density (W<sub>st</sub>), recoverable energy density (W<sub>rec</sub>) and energy storage efficiency (Π) derived from the P-E loops of the (1-x)PbHfO<sub>3</sub>-xAgNbO<sub>3</sub> ceramics as a function of the AN concentration. (c) The Weibull distribution for the (1-x)PbHfO<sub>3</sub>-xAgNbO<sub>3</sub> ceramics for the calculation of dielectric breakdown strength (DBS). (d) Comparison of the energy storage performance of (1-x)PbHfO<sub>3</sub>-xAgNbO<sub>3</sub> ceramics with x = 0.027 at room temperature with that of recently reported materials [ AN-based, NN-based, PZ/PH-based, PH-based] [11,16-18,22,31,36,41,45,58-69].

behaviour can be clearly noticed for x = 0.04. The value of DBS becomes smaller than  $E_{cr}$ , and, consequently, the transition to FE phase and double hysteresis loops are not observed, which results in a sharp decrease of  $P_{max}$ .

In order to investigate the energy-storage properties of the (1-x)PbHfO<sub>3</sub>-xAgNbO<sub>3</sub> ceramics, the areas of the loops were integrated according to Equations (1) - (3). The variations of  $W_{st}$ ,  $W_{rec}$  and  $\eta$  as a function of AN concentration are presented in Figure 15-(a-b). The highest value of  $W_{st}=9$  J/cm³ is recorded for x=0.01, whereas the highest value of  $W_{rec}=4.8$  J/cm³ is found for x=0.027. Due to the presence of a relatively wide area between the charging and discharging curves, the values of efficiency ( $\eta$ ) are rather mediocre: 51 % for x=0.01 and 58 % for x=0.27. Overall, the compositions of x=0.01 and 0.027 exhibit the best energy storage performance of the (1-x)PH-xAN solid solution.

To calculate the dielectric breakdown strength (DBS) values, the Weibull distribution formulae based on the statistical nature of failure is widely used, which can be mathematically expressed as: 54-57

$$X_{i} = ln (E_{i}), \tag{6}$$

$$Y_i = \ln (\ln(1/(1-P_i))),$$
 (7)

$$P_i = i/(n+1),$$
 (8)

where,  $X_i$  and  $Y_i$  are the parameters in the Weibull distribution function, and  $E_i$ , i and n are the specific breakdown electric field of the  $i^{th}$  specimen, the sum of specimens and the serial number of a specimen, respectively, and  $P_i$  is the polarizability. To obtain the average breakdown strength, more than eight samples of each composition were examined. Figure 15-(c) exhibits the DBS values of the  $(1-x)PbHfO_3-xAgNbO_3$  ceramics. All the data points

are found to follow the Weibull distribution function. The average breakdown strength is found to decrease from 207 to 121 kV/cm. The composition with the highest  $W_{rec}$  (x = 0.027) is found to have a DBS of 160 kV/cm.

The recoverable energy storage performance of the  $(1-x)PbHfO_3-xAgNbO_3$  solid solution with x=0.027 at room temperature is compared with that of some recently reported materials in Figure 15-(d). It can be seen that the  $0.973PbHfO_3-0.027AgNbO_3$  ceramic possesses the highest recoverable energy density at a relatively low field.

#### 3.5 Nature of the IM phase

To investigate the nature of the IM phase in the (1-x)PH-xAN solid solution, the P-E relations were measured at 10 Hz in the temperature range between 100 and 225 °C (Figure 16-(a-c)). All the compositions clearly show double hysteresis loops up to 175 °C. With further raise in temperature up to 200 °C, the loops become much slimmer, but still display the AFE characteristics. Above 200 °C, the loops become linear, which marks the feature of the PE state (Figure 16-(a)). These results indicate that all the phases below TC1, i.e. AFE1, AFE2 and IM phases, are AFE in nature, which is consistent with our structural refinement results showing the orthorhombic non-polar symmetries. The highest value of  $P_{max}$  = 25  $\mu C/cm^2$  in all the compositions is obtained in AFE<sub>2</sub> phase at the temperatures close to the transition to IM phase and it decreases sharply in the IM phase (185 - 203 °C). This behaviour confirms the existence of isostructural phase transition between AFE<sub>2</sub> and IM phases. Due to the similar results for the different compositions, only the results of a few selected compositions are displayed here. Figure 16-(d) shows the compositional dependence of W<sub>rec</sub> and η of the (1-x)PH-xAN ceramics at 175 °C. The highest value of

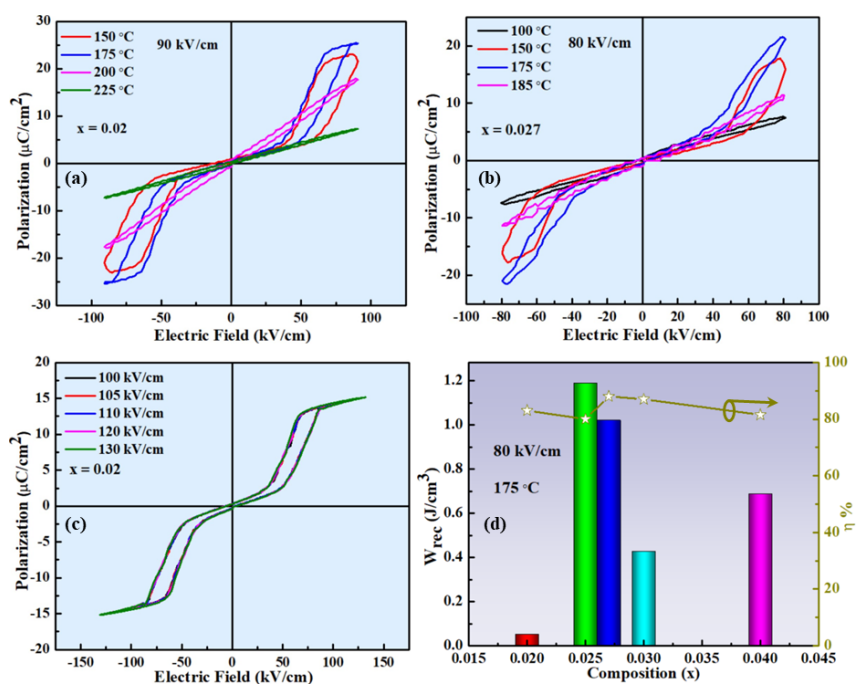


Figure 16. (a-b) Polarization-electric field (P-E) relations measured at the electric fields of  $\pm$  90 kV/cm and  $\pm$ 80 kV/cm for x = 0.02 and 0.027, respectively, at high temperatures. (c) Antiferroelectric properties of x = 0.02 measured at 175 °C at various external electric fields. (d) Variations of W<sub>rec</sub> and  $\eta$  as a function of the concentration of AN, measured at  $\pm$ 80 kV/cm.

 $W_{rec}$  = 1.19 J/cm³ is found for x = 0.025 at an applied field of 80 kV/cm. In comparison with the room temperature data, the efficiency corresponding to the highest  $W_{rec}$  is increased to 80 % (x = 0.025), whereas the critical field  $E_{cr}$  is generally reduced at 175 °C. At high temperatures the energy barrier for the transformation from the AFE and FE phase decreases, and thereby, a smaller field is required to induce the AFE to FE transition.

#### 4. Conclusions

To develop dielectric ceramics with enhanced energy storage properties for such applications as pulse power devices at low applied electric fields, a new antiferroelectric-ferrielectric solid solution (1-x)PbHfO<sub>3</sub>-xAgNbO<sub>3</sub> is designed and synthesized in the form of ceramics. The value of the critical field E<sub>cr</sub> decreases as the concentration of AN increases. A maximum polarization of 55  $\mu$ C/cm<sup>2</sup> is achieved for x = 0.027 at a relatively low applied electric field of 172 kV/cm. In comparison with other AFEs so far reported under similar electric field. The (1-x)PH-xAN ceramics with x = 0.027 exhibits the highest  $W_{rec} = 4.8 \text{ J/cm}^3$  at a low electric field of 172 kV/cm. It is also found that the partial substitution of AN for PH inhibits the grain growth, leading to the ceramics of high density. At x < 0.02 the solid solutions are found to undergo phase transitions from the AFE1 to AFE2 and then to PE phase. A new intermediate (IM) phase of AFE nature is found between the AFE<sub>2</sub> and PE phases for  $0.02 \le x \le 0.03$ . It has the same space group of Imma as the AFE2 phase. A temperature - composition (T-x) phase diagram is established. In addition, the (1-x)PH-xAN ceramics are found to exhibit good energy storage performance in a wide temperature range from 20 to 175 °C with a decent recoverable energy density (1.15 J/cm³) and a high efficiency (≥ 80%) at 175 °C. This work demonstrates that the new (1-x)PbHfO<sub>3</sub>-xAgNbO<sub>3</sub> solid solution exhibits high energy storage performance and a good thermal stability up to 175 °C, useful for a wide range multifunctional applications.

## 5. Authors Contribution

Conceptualization V.C. and Z.-G.Y.; data curation V.C.; Software V.C. and B.-X.W.; investigation V.C., A.A.B. and B-X.W.; validation, V.C., A.A.B. and Z.-G.Y.; formal analysis, V.C.; methodology, V.C. and Z.-G.Y.; resources, Z.-G.Y.; writing—original draft preparation, V.C.; writing—review and editing, Z.-G.Y. and A.A.B.; visualization, V.C. and Z.-G.Y.; supervision, Z.-G.Y.; project administration, Z.-G.Y.; funding acquisition, Z.-G.Y. All authors have read and agreed to the published version of the manuscript.

# 6. Conflicts of Interest

The authors declare no conflict of interest.

# 7. Acknowledgements

This research was funded by the Natural Sciences and Engineering Research Council of Canada (NSERC, Grant, No. RGPIN-2023-04416) and the U. S. Office of Naval Research (ONR, Grant No. N00014-21-1-2085).

# 8. References

- 1 G. Naumann, C. Cammalleri, L. Mntaschi and L. Feyen, Nat. Clim. Change, 2021, 11, 485–491.
- 2 G. Semieniuk, P. B. Holden, J. F. Mercure, P. Salas, H. Pollitt, K. Jobson, P. Vercoulen, U. Chewpreecha, N. R. Edwards and J. E. Viñuales, *Nat. Clim. Change*, 2022, 12, 532–538.
- 3 H. Gao, M. Wu, H. Liu, Y. Xu and Z. Liu, *Environ. Pollut.*, 2022, **293**, 1-10.
- 4 J. Du, W. Qv, Y. Niu, M. Qv, K. Jin, J. Xie and Z. Li, J. Hazard. Mater., 2022, 424, 1-9.
- T. Hasegawa, S. Fujimori, P. Havlík, H. Valin, B. L. Bodirsky, J. C. Doelman, T. Fellmann, P. Kyle, J. F. L. Koopman, H. Lotze-Campen, D. Mason-D'Croz, Y. Ochi, I. P. Domínguez, E. Stehfest, T. B. Sulser, A. Tabeau, K. Takahashi, J. Takakura, H. Meijl, W. J. Zeist, K. Wiebe and P. Witzke, Nat. Clim. Change, 2018, 8, 699–703.
- 6 Energy Storage Grand Challenge: Energy Storage Market Report, The U.S. Department of Energy, *Technical Report* NREL/TP, 2020, 5400-78461.
- 7 Y. Bo, Q. Zhang, H. Cui, M. Wang, C. Zhang, W. He, X. Fan, Y. Lv, X. Fu, J. Liang, Y. Huang, R. Ma and Y. Chen, *Adv. Energy Mater.*, 2021, **11**, 1–8.
- 8 Z. Wu, X. Liu, C. Ji, L. Li, S. Wang, Y. Peng, K. Tao, Z. Sun, M. Hong and J. Luo, *J. Am. Chem. Soc.*, 2019, **141**, 3812–3816.
- Y. Bao, X. Dong and G. Wang, ACS Appl. Energy Mater., 2019, 2, 6939–6951.
- 10 Z. Yao, Z. Song, H. Hao, Z. Yu, M. Cao, S. Zhang, M. T. Lanagan and H. Liu, *Adv. Mater.*, 2017, **29**, 1-15.
- 11 N. Luo, K. Han, M. J. Cabral, X. Liao, S. Zhang, C. Liao, G. Zhang, X. Chen, Q. Feng, J. F. Li and Y. Wei, *Nat. Commun.*, 2020, **11**, 1–10.
- 12 Q. Li, L. Chen, M.R. Gadinski, S. Zhang, G. Zhang, H. Li, A. Haque, L. Q. Chen, T. Jackson and Q. Wang, *Nature*, 2015, **523**, 576–579.
- 13 J. Li, F. Li, Z. Xu and S. Zhang, Adv. Mater., 2018, 30, 1-7.
- 14 Z. Liu, T. Lu, J. Ye, G. Wang, X. Dong, R. Withers and Yun Liu, Adv. Mater. Technol., 2018, 3, 1–21.
- Z. Ye, X. Hao and Q. Zhang, ACS Appl. Mater. Interfaces, 2014, 6, 11633-11639.
- 16 S. Li, H. Nie, G. Wang, C. Xu, N. Liu, M. Zhou, F. Cao and X. Dong, J. Mater. Chem. C, 2019, 7, 1551–1560.
- 17 N. Luo, K. Han, F. Zhuo, C. Xu, G. Zhang, L. Liu, X. Chen, C. Hu, H. Zhou and Y. Wei, J. Mater. Chem. A, 2019, 7, 14118–14128.
- 18 P. Gao, Z. Liu, N. Zhang, H. Wu, A. A. Bokov, W. Ren and Z.-G. Ye, Chem. Mater., 2019, 31, 979–990.
- 19 T. Haixiong and H. A. Sodano, *Nano Lett.*, 2013, **13**, 1373–1379.
- 20 Z. Wang, R. Kang, L. Zhang, P.u. Mao, Q. Sun, F. Kang and J. Wang, J. Eur. Ceram. Soc., 2021, 41, 1917–1924.
- 21 J. H. Gao, Y. Wang, Y. B. Liu, X. H. Hu, X. Q. Ke, L. S. Zhong, Y. T. He and X. B. Ren, Sci. Rep., 2017, 7, 40916-40916.
- 22 J. Gao, Y. Zhang, L. Zhao, K. Lee, Q. Liu and A. Studer, *J. Mater. Chem. A*, 2019, **7**, 2225–2232.
- 23 X. Yang, F. Zhuo, C. Wang, Y. Liu, Z. Wang, H. Tailor, C. He and X. Long, *J. Mater. Chem. A*, 2019, **7**, 8414–8422.
- 24 J. Guo and T. Yang, J. Alloys Compd., 2021, 888, 1-7.
- 25 X. Liu, Y. Zhao, N. Sun, Y. Li and X. Hao, *J. Chem. Eng.*, 2021, **417**, 1-9.

- 26 S. Li, T. Hu, H. Nie, Z. Fu, C. Xu, F. Xu, G. Wang and X. Dong, Energy Storage Mater., 2021, 34, 417–426.
- 27 H. Cai, S. Yan, M. Zhou, N. Liu, J. Ye, S. Li, F. Cao, X. Dong and G. Wang, J. Eur. Ceram. Soc., 2019, 39, 4761–4769.
- 28 Z. Lin, Y. Chen, Z. Liu, G. Wang, D. Rémiens and X. Dong, J. Eur. Ceram., 2018, 38, 3177–3181.
- 29 P. Z. Ge, X. G. Tang, K. Meng, X. X. Huang, Q. X. Liu, Y. P. Jiang, W. P. Gong and T. Wang, *Mater. Today Phys.*, 2022, **24**, 1-9.
- 30 P. Z. Ge, X. G. Tang, K. Meng, X. X. Huang, S. F. Li, Q. X. Liu and Y. P. Jiang, *J. Chem. Eng.*, 2022, **429**, 1-9.
- 31 N. Luo, K. Han, F. Zhuo, L. Liu, X. Chen, B. Peng, X. Wang, Q. Feng and Y. Wei, *J. Mater. Chem. C.*, 2019, **7**, 4999–5008.
- 32 J. Gao, L. Zhao, Q. Liu, X. Wang, S. Zhang and J. F. Li, J. Am. Ceram. Soc., 2018, **101**, 5443–5450.
- 33 H. Qi and R. Zuo, J. Mater. Chem. A, 2019, 7, 3971–3978.
- 34 X. Dong, X. Li, X. Chen, H. Chen, C. Sun, J. Shi, F. Pang and H. Zhou, *J Materiomics.*, 2021, **7**, 629–639.
- 35 Z. Ren, N. Zhang, L. W. Su, H. Wu and Z. -G. Ye, *Appl. Phys.*, 2014, **116**, 1–6.
- 36 H. Wan, Z. Liu, F. Zhuo, J. Xi, P. Gao, K. Zheng, L. Jiang, J. Xu, J. Li, J. Zhang, J. Zhuang, G. Niu, N. Zhang, W. Ren and Z.- G. Ye, J. Mater. Chem. A, 2023, 11, 25484–25496.
- 37 G. Baldinozzi, P. Sciau, M. Pinot and D. Grebille, *Acta. Crystallogr. B*, 1995, **51**, 668–673.
- 38 A. K. Tagantsev, K. Vaideeswaran, S. B. Vakhrushev, A. V. Filimonov, R. G. Burkovsky, A. Shaganov, D. Andronikova, A. I. Rudskoy, A. Q. R. Baron, H. Uchiyama, D. Chernyshov, A. Bosak, Z. Ujma, K. Roleder, A. Majchrowski, J. H. Ko and N. Setter, *Nat. Commun.*, 2013, **4**, 1-8.
- 39 A. Bosak, V. Svitlyk, A. Arakcheeva, R. Burkovsky, V. Diadkin, K. Roleder and D. Chernyshov, Acta. Crystallogr. B. Struct., 2020, 76, 7–12.
- 40 D. L. Corker, A. M. Glazer, W. Kaminsky, R. W. Whatmore, J. Dec and K. Roleder, *Acta. Crystallogr. B. Struct.*, 1998, **54**, 18–28.
- 41 V. Chauhan, B. Wang and Z.-G. Ye, Materials, 2023, 16, 1-14.
- 42 B. F. Swaringen, E. Gawlik, G. D. Kamenov, N. E. McTigue, D. A. Cornwell and J. B. Claude, *Environ. Res.*, 2022, **204**, 1-18.
- 43 I. Manisalidis, E. Stavropoulou, A. Stavropoulos and E. Bezirtzoglou, *Front. Public Health*, 2020, **8**, 1–13.
- 44 A. L. Wani, A. Ara and J. A. Usmani, *Interdiscipl. Toxicol.*, 2015, **8**, 55–64.
- 45 L. Zhao, Q. Liu, S. Zhang and J.-F. Li, *J. Mater. Chem. C*, 2016, **4**, 16-18.
- 46 M. Yashima, S. Matsuyama, R. Sano, M. Itoh, K. Tsuda and D. Fu, Chem. Mater., 2011, 23, 1643–1645.

- 47 D. Fu, M. Endo, H. Taniguchi, T. Taniyama and M. Ltoh, *Appl. Phys. Lett.*, 2007, **90**, 20–23.
- 48 D. Viehland, D. Forst, Z. Xu and J. F. Li, *J. Am. Ceram. Soc.*, 1995, **78**, 2101–2112.
- 49 G. Shirane, R. Pepinsky and B. C. Frazer, *Acta Crystallogr.*, 1956, 9, 131–140.
- 50 M. F. Kupriyanov, E. V. Petrovich, E. V. Dutova and Y. V. Kabirov, *Crystallogr. Rep.*, 2012, **57**, 205–207.
- 51 P. Gao, C. Liu, Z. Liu, H. Wan, Y. Yuan, H. Li, Y. Pu and Z.-G. Ye, J. Eur. Ceram. Soc., 2022, **42**, 1370–1379.
- 52 A.M. Glazer, Acta Cryst., 1972, 28, 3384–3392.
- 53 S. C. Vogel, J. Appl. Crystallogr., 2011, 44, 873-877.
- 54 J. Chen, Y. Zhang, C. Deng, X. Dai and L. Li, *J. Am. Ceram. Soc.*, 2009, **92**, 1350–1353.
- 55 J. Huang, Y.Zhang, T. Ma, H. Li and L. Zhang, *Appl. Phys. Lett.*, 2010, **96**, 1-3.
- 56 L. Zhao, Q. Liu, J. Gao, S. J. Zhang and J. F. Li, *Adv. Mater.*, 2017, **29**, 1-7.
- 57 L. Zhao, J. Gao, Q. Liu, S. Zhang and J. Li, ACS Appl. Mater. Interfaces, 2018, 10, 819–826.
- 58 J. Gao, L. Zhao, Q. Liu, X. Wang, S. Zhang and J. F. Li, J. Am. Ceram. Soc., 2018, 101, 5443–5450.
- 59 M.X. Zhou, R. H. Liang, Z. Y. Zhou and X. L. Dong, *J. Mater. Chem. A*, 2018, **6**, 17896–17904.
- 60 S. Mao, N. Luo, K. Han, Q. Feng, X. Chen, B. Peng and L. Liu, J. Mater. Sci. Mater, 2020, 31, 7731–7741.
- 61 Y. Wang, S. Gao, T. Wang, J. Liu, D. Li, H. Yang, G. Hu, L. Kong, F. Wang and G. Liu, *Ceram. Int.*, 2020, **46**, 12080–12087.
- 62 K. Han, N. Luo, S. Mao, F. Zhuo, X. Chen, L. Liu, C. Hu, H. Zhou, X. Wang and Y. Wei, *J. Materiomics.*, 2019, **5**, 597–605.
- 63 Y. Tian, L. Jin, Q. Hu, K. Yu, Y. Zhuang, G. Viola, I. Abrahams, Z. Xu, X. Wei and H. Yan, *J. Mater. Chem. A*, 2019, **7**, 834–842.
- Ku, X. Wei and H. Hall, J. Mater. Chem. A, 2013, 7, 834–842.
   K. Han, N. Luo, S. Mao, F. Zhuo, L. Liu, B. Peng, X. Chen, C. Hu, H. Zhou and Y. Wei, J. Mater. Chem. A, 2019, 7, 26293–26301.
- 65 X. Zhang, D. Hu, Z. Pan, X. Lv, Z. He, F. Yang, P. Li, J. Liu and J. Zhai, *J. Chem. Eng.*, 2021, **406**, 1–9.
- 66 T. Shao, H. Du, H. Ma, S. Qu, J. Wang, J. Wang, X. Wei and Z. Xu, J. Mater. Chem. A, 2017, 5, 554–563.
- 67 Z. Yan, D. Zhang, X. Zhou, H. Qi, H. Luo, K.Zhou, I. Abrahams and H. Yan, *J. Mater. Chem. A*, 2019, **7**, 10702–10711.
- 68 H. Wang, Q. Hu, X. Liu, Q. Zheng, N. Jiang, Y. Yang, K. W. Kwok, C. Xu and D. Lin, *Ceram. Int.*, 2019, **45**, 23233–23240.
- 69 H. Xu, Y. Dan, K. Zou, G. Chen, Q. Zhang, Y. Lu and Y. He, J. Mater. Res. Technol., 2019, **8**, 3291–3296.

# Journal of Materials Chemistry A

Manuscript ID: TA-ART-04-2024-002493

TITLE: Achieving Ultrahigh Energy Storage Density at Low Operating Fields in Lead Hafnate-

Based Novel Perovskite Solid Solutions

Authors: Vidhi Chauhan, Bi-Xia Wang, Alexei A. Bokov, Zuo-Guang Ye \*

# **Data Availability Statement**

The raw data required and processed to reproduce these findings are available from the corresponding author upon reasonable request.